Influence of the source of yttrium on the morphology of precipitated phases after interaction with a CaO-Al2O3-SiO2 melt at 1300°C

J. Bonnal, Carine Petitjean, Pierre-Jean Panteix, L. Saint-Jean, David Bonina, S. Arnal, Michel Vilasi

Influence of the source of yttrium on the morphology of precipitated phases after interaction with a CaO-Al_2O_3-SiO_2 melt at 1300°C

J. Bonnal[1,2], C. Petitjean[1], P.J. Panteix[1*], L. Saint-Jean[1], D. Bonina[1], S. Arnal[3], M. Vilasi[1]

[1]Université de Lorraine, CNRS, IJL, F-54000 Nancy, France

[2]Safran Aircraft Engines, 91000 Corbeil-Essonnes, France

[3]Safran Ceramics, 33700 Mérignac, France

[*]corresponding author. *E-mail address:* pierre-jean.panteix@univ-lorraine.fr

Abstract

The durability of the ceramic coatings used to protect the turbine blades in the field of aeronautical engines is strongly linked to their ability to withstand corrosion by calcium-magnesium-aluminosilicates (i.e. CMAS), which can infiltrate their microstructure when liquid at high temperature. Protection can be provided thanks to the high reactivity of the ceramic coatings with CMAS leading to the fast precipitation of protective phases. Most ceramic coatings contain rare-earth elements (e.g. rare-earth monosilicates RE_2SiO_5 or rare-earth disilicates $RE_2Si_2O_7$), making them thus able to form oxyapatite after reaction with the silicate melts. The present works proposes to study the morphology of these precipitated phases depending on the nature of the rare-earth source. A model ternary melt CaO-Al_2O_3-SiO_2 has thus been put in contact at 1300°C with different sources of yttrium: oxide Y_2O_3, monosilicate Y_2SiO_5 and disilicate $Y_2Si_2O_7$. The reactivity led to the precipitation of the two phases of interest (i.e. apatite $Ca_2Y_8(SiO_4)_6O_2$ and cyclosilicate $Ca_3Y_2(Si_3O_9)_2$). The use of these simplified systems allows to establish the precipitation mechanisms of the phases at equilibrium regarding previously established phase diagrams. Depending on the yttrium source, the chemical reactions involved local modifications of the melt composition, which strongly influenced the morphology of the precipitated phases at equilibrium. Specifically, it is demonstrated here that the release of SiO_2 in the melt when starting from yttrium disilicate involves a specific microstructure of the acicular apatite, which exhibits a core containing precipitated SiO_2.

Keywords

Rare-earth ; ceramic coatings ; molten silicate ; apatite; reactivity ; corrosion

1. Introduction

In the context of aeronautical engines, an important challenge is the lowering of their environmental impact thanks to a decrease of their fuel consumption and release of greenhouse gases. This involves the development of new materials and coatings. Rare-earth-based ceramics are very promising materials as thermal and environmental barrier coatings (i.e. E/TBCs) [1]. However, these coatings are the first to be in contact with molten siliceous deposits resulting from the ingestion of mineral particles during in-flight operation. These particles, which are comprising sands, dust or volcanic ashes, are mainly constituted of calcia CaO, magnesia MgO, alumina Al_2O_3 and silica SiO_2, and known as CMAS [1-4]. These oxide mixes lead to liquid silicates at high temperature (here higher than 1200°C). Consequently, the thermochemical degradation consists in (i) the acido-basic dissolution of the ceramic in the melt and (ii) the precipitation of new phases [5-9]. It has also been evidenced that protection of the ceramic barrier coatings could be provided by the fast precipitation of some of these phases at the interface with the liquid silicate [6,7]. For example, in the case of Thermal Barrier Coatings (i.e. TBCs) made of gadolinium zirconate $Gd_2Zr_2O_7$, the fast precipitation of apatite $Ca_2Gd_8(SiO_4)_6O_2$ and zirconia ZrO_2 is observed.

The fast precipitation of rare-earth oxyapatites has been previously verified [10-12] and is a relevant criterion to underline the protective properties of this phase. Apatite has hexagonal crystallographic structure (space group $P6_3/m$) with general formula $Me_{10}(XO_4)_6Z_2$ [13]: Me represents a divalent cation, XO_4 a trivalent anion and Z a monovalent anion. Me^{2+} cations are located in two different sites: four Me_I are at the centre of narrow tunnels (4f sites), six Me_{II} around large tunnels (6h sites) the centers of which are occupied by Z^- anions (2a sites). The coordination number of Me_I site is nine, whereas for Me_{II}, it is only seven [13]. A lot of substitutions can be observed in the apatite structure, with elements having valences differing from the general formula noted above. It is the case of rare-earth oxyapatite with a punctual defect free formulation $Ca_2RE_8(SiO_4)_6O_2$ where Me = Ca^{2+} or RE^{3+}, XO_4 = SiO_4^{4-} and Z = O^{2-}. Substitutions are possible between the Ca^{2+} and RE^{3+} cations, the electric charge being compensated by the creation of cation vacancies or punctual defects on 2a sites (vacancies or interstitial oxygen atoms). Thus, the domain of existence of the phase is limited on one side by a formulation with no calcium $RE_{9.33}\square_{0.67}(SiO_4)_6O_2$, and on the other side by a formulation with four atoms of calcium occupying all the 4f sites, the electric charge being compensated by one oxygen vacancy in 2a site $Ca_4RE_6(SiO_4)_6O\square$ [14].

The formation mechanism of apatite is often described in two steps: first the rare-earth source dissolves in the melt before leading to precipitation of apatite [10-12,15-17]. The morphology of the phase has also to be taken into account in order to consider the efficiency of the protection against corrosion by a liquid phase. Indeed, it should form a compact layer at the surface of the barrier coating, with the ability to avoid or mitigate the melt infiltration. Due to their crystal structure described above, rare-earth oxyapatites precipitated in liquid silicates most often exhibit acicular shape with hexagonal section [10-12,15-22]. Many parameters can have an influence on the apatite formation process. For example, increasing the temperature during contact between CMAS and yttrium disilicate leads to thicker apatite layers with more acicular shape of the precipitated grains [15,16]. This influence is less significant beyond 1400°C as the fast formation of apatite induces a fast depletion of calcium from the melt, stopping further apatite precipitation [15]. The nature of the rare-earth present in the starting disilicate is also of importance and has been studied by several authors [12,15,20,21]. Guo et

al [12] consider three main criteria : (i) the reactivity of the rare-earth disilicate, as a fast precipitation is important to provide protection in the first moments of interaction with the melt, (ii) a low solubility of the rare-earth element and (iii) a low wettability of the melt on the rare-earth disilicate in order to limit the surface of the interaction. Among several lanthanides, intermediate elements as Sm and Gd exhibited the best compromise based on these criteria. The precipitation of apatite is not always verified, as in the case of Sc where it is never detected [12,18]. Furthermore, rare-earth element with high basicity (i.e. high ionic radius) are often presented as favoring the precipitation of apatite [11,21]. In the case of the more acidic rare-earths, e.g. ytterbium, the precipitation can be much more favored by using ytterbium monosilicate Yb_2SiO_5 as starting material [17,19,23]. Yttrium disilicate seems more reactive than ytterbium monosilicate [22]. The stoichiometry of apatite can be influenced by the rare-earth source, $Y_2Si_2O_7$ and Yb_2SiO_5 giving rare-earth rich and calcium rich apatites respectively. In the same way, for a given CMAS melt, basic rare-earth elements tend to induce the precipitation of calcium rich apatites [21]. Coprecipitation of other phases can also be observed when starting from $YAlO_3$ which leads to coprecipitation of garnet $Y_3Al_5O_{12}$ [24]. Lastly, the composition of the melt is of importance, specifically the Ca/Si ratio which drives the reactivity with the rare-earth sources, since the melt brings the calcium required for the precipitation of apatite [16,17,21,23]. The formation of apatite due to reaction between a melt and a rare-earth disilicate has been quoted to locally enrich the melt in Si, leading to a loose morphology of the precipitated apatite agglomerates [16,17]. Melts with low CaO content also exhibit lower reactivity for apatite formation [23]. It has also been shown through image analyses that in the case of Nd, Gd and Dy disilicates interacting at 1400°C with CMAS of different compositions, the more acidic (SiO_2 rich) melts led to apatite needles with higher acicularity (i.e. high acicular ratio c/a = length/diameter) [21].

This study proposes to specifically study the morphology of the precipitated phases formed when one rare-earth element, in this case yttrium, is brought by three sources: yttrium oxide Y_2O_3, monosilicate Y_2SiO_5 (noted here as MSY) and disilicate $Y_2Si_2O_7$ (noted here as DSY). Interactions are performed at 1300°C with a simplified ternary melt CaO-Al_2O_3-SiO_2. A wide range of CMAS compositions has already been reported [25], with various proportions of CaO, Al_2O_3 and SiO_2, and all of them contain Mg and Fe oxides which can strongly influence the melt reactivity and the nature of the precipitated phases. Consequently, such a simplified Mg and Fe-free composition has been chosen in order to have a steady approach of the influence of the nature of the rare-earth source.

The aim here is to provide a sound understanding of the precipitation phenomena of the reactions products. The discussions will be based on thermodynamic equilibrium considerations previously reported in the CaO-SiO_2-$YO_{1.5}$ added with Al_2O_3 [26]. Furthermore, the reactivity of the three sources of yttrium will be regarded through their ability to form apatite $Ca_2Y_8(SiO_4)_6O_2$ and cyclosilicate $Ca_3Y_2(Si_3O_9)_2$ phases with different morphologies when interacting with a CaO-Al_2O_3-SiO_2 melt. Characterizations performed by STEM and EPMA give access to accurate observations and quantifications in the melt, providing information on the precipitation of the equilibrium phases.

2. Materials and methods

2.1. Samples preparation

The simplified melt selected for this study corresponds to the pseudo-ternary eutectic (1170°C) composition of the CaO-Al_2O_3-SiO_2 system. It is noted here as CAS, and its theoretical composition is reported in Table 1.

Table 1. Theoretical and measured composition of ternary CAS melt.

Composition (mol.%)	CaO	Al_2O_3	SiO_2
theoretical	26.40	9.20	64.40
measured by EPMA	28.58	9.40	62.02

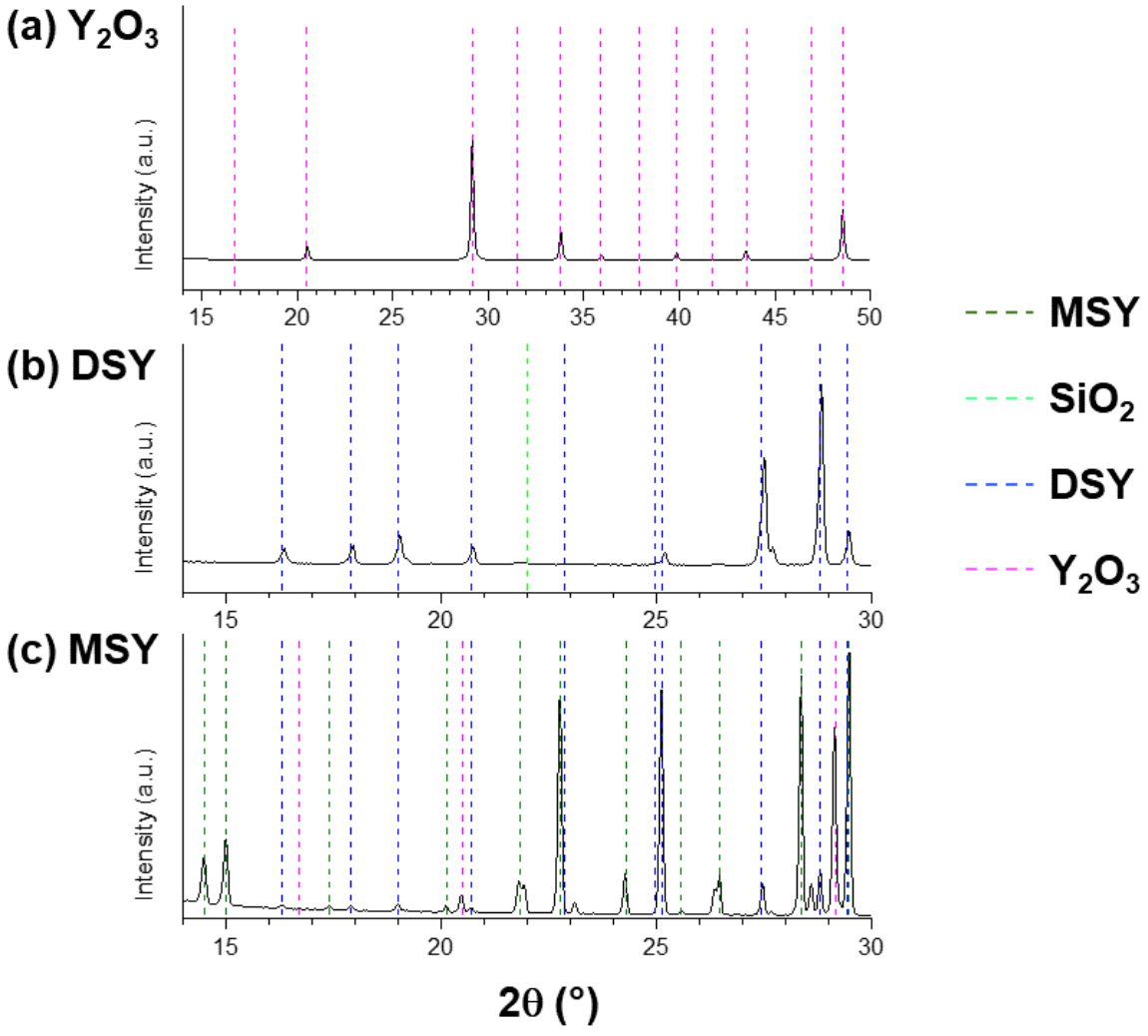

Figure 1. X-ray diffraction patterns of reagents powders of yttrium oxide Y_2O_3 (a), yttrium disilicate $Y_2Si_2O_7$ (b), and yttrium monosilicate Y_2SiO_5 (c).

The melt was prepared from a mixture of appropriate amounts of high purity (> 99%) oxides (SiO_2 and Al_2O_3) and carbonates ($CaCO_3$) provided by Sigma Aldrich. After ethanol-wet

milling, the reagents mixture was heated at 1500°C for 12 hours (heating rate = 2°C per min) and then water quenched. The obtained glass was finally ground down to a granulometry of D_{50} = 30 µm. The composition of the synthesised glass was measured by Electron Probe MicroAnalysis (EPMA) and is also reported in Table 1. It is relatively close to the expected composition, despite a CaO content slightly higher to the detriment of SiO_2.

Yttrium oxide Y_2O_3 (99.9% Thermo Fischer), yttrium disilicate $Y_2Si_2O_7$ (Marion Technologies), and yttrium monosilicate Y_2SiO_5 (Marion Technologies) were used as yttrium sources. X-ray diffraction patterns of the three powders are reported in Figure 1 (Bruker D8 Advance diffractometer with CuKα radiation - λ = 0.15406 nm; diffractograms recorded between 15° and 80° with steps of 0.021°, total acquisition time = 2 h).

As seen on Figure 1(a), yttrium oxide Y_2O_3 is the only single-phased powder. On Figure 1(b) allotropic forms γ-$Y_2Si_2O_7$ and β-$Y_2Si_2O_7$ of yttrium disilicate can be distinguished with a very small amount of cristobalite SiO_2 (peak at 2θ = 22°). A purity of 99.6% is given by semi-quantitative analysis. Yttrium monosilicate shown on Figure 1(c) exhibits the lowest purity, since significant amounts of γ-$Y_2Si_2O_7$ and Y_2O_3 are detected in the main X-Y_2SiO_5 phase. A

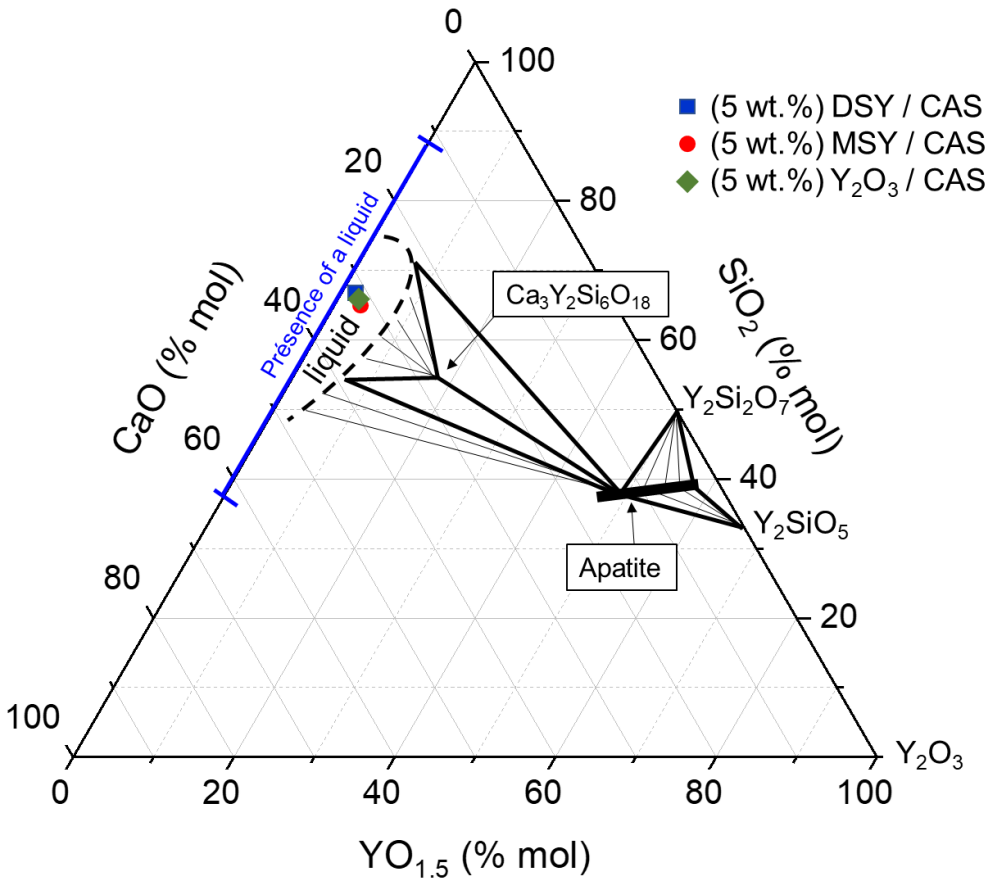

semi-quantitative analysis gives an amount of 82.8% of Y_2SiO_5.

Figure 2. Theoretical compositions of the CAS samples added with 5 wt.% of DSY, MSY and Y_2O_3 reported in the modified ternary phase diagram $CaO\text{-}SiO_2\text{-}YO_{1.5}$ added with 9 mol.% Al_2O_3 at 1300°C [26].

The interaction of yttrium oxide (Y_2O_3) and silicates (monosilicate Y_2SiO_5 and disilicate $Y_2Si_2O_7$) with CAS has been studied according to a procedure described previously [10]. CAS glass was crushed and mixed with the same proportion of yttrium source (5 wt.%, in the three cases). The three initial states reported in the previously published modified phase diagram of the ternary system $CaO\text{-}SiO_2\text{-}YO_{1.5}$ added with 9 mol.% Al_2O_3 at 1300°C [26] in Figure 2, which shows that all of them are located in the liquid area. The large volume of CAS involves a limitation of the interactions between aggregates.

The mix was then heated at 1300°C for 3 minutes (long enough to melt the CAS), air quenched and crushed, this operation being performed twice in order to ensure the homogeneity of the dispersion of the yttrium source in the glass. Calibrated spherical samples (4 mm diameter) with reproducible surface/volume ratio were then prepared by heating chosen pieces of 140 mg of the mix at 1300°C for 1 minute in a graphite crucible. The obtained samples were lastly sustained with a Pt wire and annealed at 1300°C in air for times up to 4 hours. The samples were air-quenched in order to characterize their high-temperature configuration. Short term heat treatments were chosen as local equilibria will be studied with no will to attain global equilibrium in the samples.

2.2. Characterization

After being embedded in epoxy resin, the samples were mirror polished. The cross sections were observed by using a Scanning Electron Microscope JEOL JSM-6010 LA (voltage = 15 kV, working distance = 10 mm).

The samples were prepared as thin sections (about 100 nm thick) by using a Focused Ion Beam (FIB) device for observation by Scanning Transmission Electron Microscopy. These observations were performed in Bright Field mode (STEM-BF) on a JEOL JEM-ARM200F. Energy Dispersive X-Ray Spectroscopy (EDS) was performed on the same device, with a voltage of 200 kV and an intensity of 0.8 nA. The Kα lines of Al, Si, Ca and Y were considered with energies respectively equal to 1.486 keV, 1.739 keV, 3.690 keV and 14.931 keV.

The compositions of the glassy matrix were determined through Electron Probe MicroAnalysis (EPMA) measurements performed on a JEOL JXA-8530F. The conditions used for the analyses were an acceleration voltage of 15 kV and a beam intensity of 20 nA, the acquisition times were 10 s and 15 s for peaks and background respectively. The standards used were wollastonite $CaSiO_3$ for Ca, albite $NaAlSi_3O_8$ for Al and Si, and yttrium disilicate $Y_2Si_2O_7$ for Y. Oxygen concentration was calculated by stoichiometry assuming that the valences states of cations are 2, 3, 4 and 3 for Ca, Al, Si and Y respectively. The results of the quantifications are averaged from 10 measurements and the error bars correspond to standard deviation.

3. Results

3.1. Interaction of CAS with $Y_2Si_2O_7$

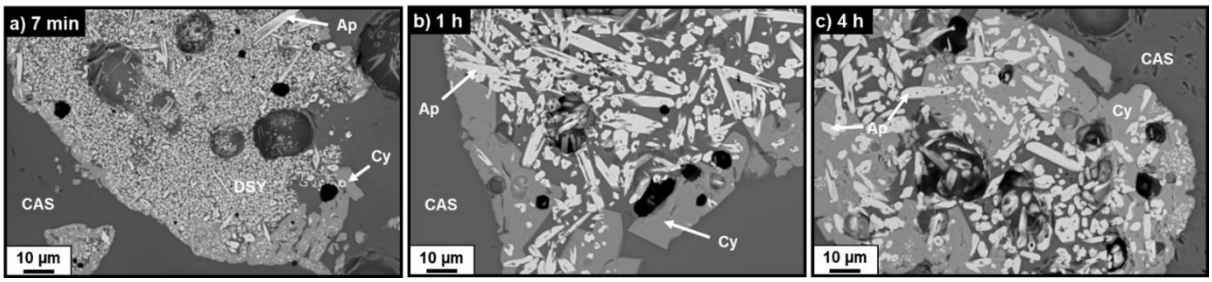

Figure 3. SEM micrographs (Back Scattered Electrons mode) of a CAS samples added with 5 wt.% $Y_2Si_2O_7$ (DSY) after 7 min (a), 1 h (b) and 4 h (c) of interaction at 1300°C.

Figure 3 presents micrographs of different times of interaction (7 minutes to 4 hours) of yttrium disilicate $Y_2Si_2O_7$ with CAS at 1300°C. Several aggregates are observed in all samples, with some bubbles due to the presence of air trapped between the grains of ceramic and glass powders before melting. Even for short times, dissolution of yttrium disilicate in the melt is detected by EDS. As equilibrium does not exist between the disilicate and the molten silicate with initial CAS composition (as seen in Figure 2 [26]), yttria-rich phases precipitate at their interface. After 7 minutes of interaction (Figure 3a), apatite $Ca_2Y_8(SiO_4)_6O_2$ and cyclosilicate $Ca_3Y_2(Si_3O_9)_2$ phases are identified. The dissolution/precipitation mechanism has previously been emphasised in the literature in the case of several rare-earth monosilicates and disilicates [2,5,15-17,27,28]. The micrograph after 7 minutes of interaction (Figure 3a) also shows that $Y_2Si_2O_7$ is not totally dissolved.

After 1 hour of interaction (Figure 3b), yttrium disilicate present in the initial mix has totally dissolved in the melt, and the apatite and cyclosilicate phases have grown. For longer interaction times (4 hours, Figure 3c), fewer precipitates are detected. The growth of the cyclosilicate phase prevails over apatite. Similar results are observed after 8 hours of interaction between yttrium disilicate and CAS at 1300°C: the nature and morphology of the phases, identified by SEM and EPMA are strictly identical to what is observed after 4 hours of observation. On these micrographs, the cyclosilicate phase is always in contact with the liquid silicate for all interaction durations. Starting from 1 hour, the same specific agglomerate morphology is observed, in which apatite needles and the liquid silicate are surrounded by cyclosilicate grains. This agglomerated morphology can be explained by the dissolution mechanism of yttrium disilicate. Indeed, it leads to a local enrichment of the liquid in SiO_2 and Y_2O_3, allowing the existence of apatite (i.e. equilibrium between SiO_2, apatite and $Y_2Si_2O_7$ [14,26]) in the ternary diagram $CaO\text{-}SiO_2\text{-}YO_{1.5}$. In this case a SiO_2-enriched liquid is observed instead of crystallised silica, due to the presence of alumina Al_2O_3 in the system.

The cyclosilicate phase grows outward the agglomerate, towards the zone where the liquid is CaO-rich, thus providing the calcium required to form cyclosilicate. The morphology of the apatite phase seems to be linked to the phase in contact with it. Indeed, apatite needles are quite long (high acicular ratio c/a = length/diameter). As the amount of cyclosilicate increases with time, the acicularity of apatite decreases. A darker contrast (BSE mode) is observed at the centre of the apatite needles, showing a different composition in the core of the phase.

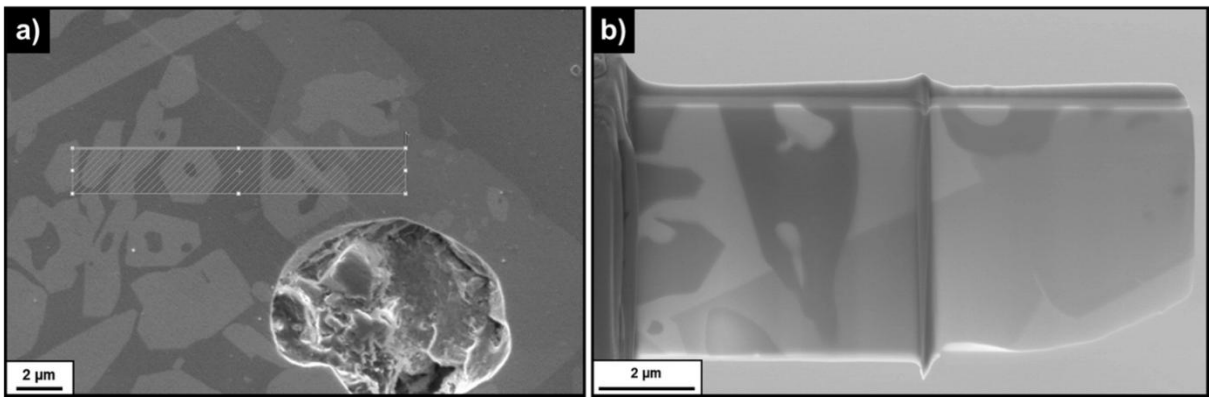

Figure 4. SEM micrographs (Secondary Electrons mode) of a CAS sample added with 5 wt.% (DSY) after 1 h of interaction at 1300°C (a) and of the FIB sample extracted from the hatched area (b)

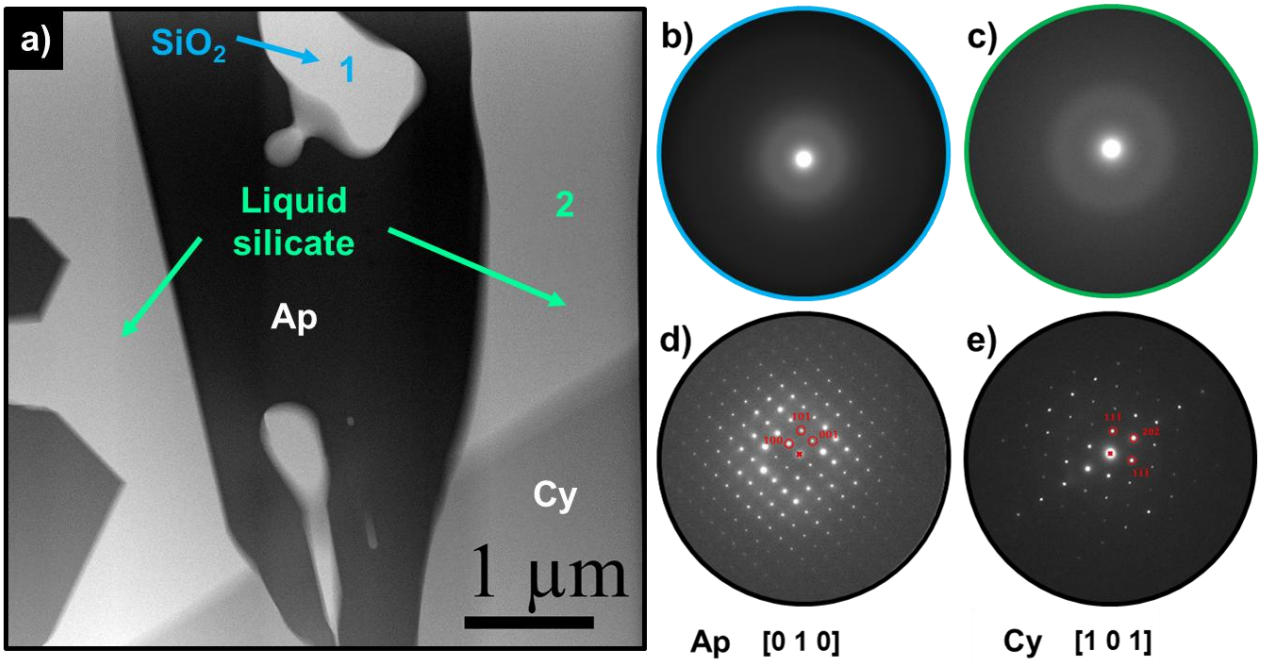

Figure 5. STEM-BF micrograph of the center of an agglomerate of a CAS sample added with 5 wt.% (DSY) after 1 h of interaction at 1300°C (a), and diffraction patterns of zone 1 (b), zone 2 (c), and of apatite (d) and cyclosilicate (e) phases.

The inner part of an agglomerate has been analysed by Scanning Transmission Electron Microscopy STEM. A sample has been prepared Focused Ion Beam (FIB) after 1 hour of interaction between CAS and yttrium disilicate at 1300°C, as shown in Figure 4. Four phases are evidenced in the bright mode micrograph detailed in Figure 5a. Diffraction patterns

performed in zones 1 (Figures 5b) and zone 2 (Figure 5c) show that both zones consist in amorphous phases. The two other zones are crystallised. The first phase has a hexagonal structure with an identified [0 1 0] zone axis (Figure 5d), and the second phase has a monoclinic structure with an identified [1 0 1] zone axis (Figure 5e). By coupling with EDS analysis (Table 2) of their compositions, the two phases are clearly identified as yttrium oxyapatite $Ca_2Y_8(SiO_4)_6O_2$ and yttrium cyclosilicate $Ca_3Y_2(Si_3O_9)_2$ respectively. The amorphous zone at the core of the apatite phase is also identified as pure silica SiO_2, and the amorphous phase in contact with both apatite and cyclosilicate has a composition close to the initial CAS, lightly enriched in yttria.

Table 2. EDS composition analysis (mol.%) of the different zones identified in Figure 5a

mol.%	CaO	Al_2O_3	SiO_2	Y_2O_3
amorphous zone 1	0	1	99	0
amorphous zone 2	24	10	64	2
apatite	16	0	50	34
cyclosilicate	29	0	61	10

3.2. Interaction of CAS with Y_2O_3 and Y_2SiO_5

In this part, the interactions at 1300°C of CAS with yttrium oxide Y_2O_3 and yttrium monosilicate Y_2SiO_5 are observed here in order to determine the influence of the yttrium source on the equilibria and the modification of the liquid silicate.

Figure 6 represents BSE micrographs of samples of Y_2O_3 mixed with CAS and quenched after 7 minutes, 1 hour and 4 hours of interaction at 1300°C. After a few minutes of interaction (Figure 6a), precipitates of apatite and cyclosilicate are observed. Y_2O_3 grains with bright contrast are surrounded by apatite needles: there is no equilibrium between Y_2O_3 and the liquid. The precipitated cyclosilicate phase is directly in contact with the melt. These local equilibria (i) Y_2O_3-apatite and (ii) liquid-cyclosilicate are consistent with the thermodynamic predictions of the ternary phase diagram $CaO\text{-}SiO_2\text{-}YO_{1.5}$ at 1400°C proposed by Poerschke et al. [14]. The cyclosilicate phase surrounds the precipitation zone of apatite and its morphology is similar to the agglomerate observed in the case of DSY-CAS samples (Figure 3).

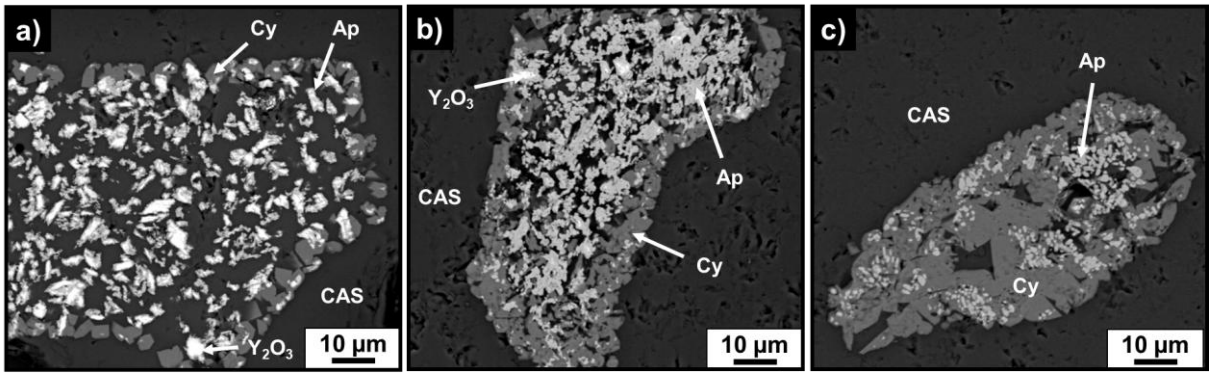

Figure 6. SEM micrographs (Back Scattered Electrons mode) of a CAS samples added with 5 wt.% Y_2O_3 after 7 min (a), 1 h (b) and 4 h (c) of interaction at 1300°C.

Only a little amount of Y_2O_3 is still observed after 1 hour of interaction (Figure 6b), as it almost totally dissolved in the melt. The growth of cyclosilicate and apatite is also observed. After 4 hours at 1300°C (Figure 7c), the growth of cyclosilicate seems to prevail over apatite, as in the case of DSY-CAS samples (Figure 3c). In the case Y_2O_3-CAS interaction, the morphology of apatite does not exhibit dark contrast in the core of the precipitated grains.

Figure 7 represents micrographs of different times of interaction (7 minutes to 4 hours) of yttrium monosilicate Y_2SiO_5 with CAS at 1300°C (initial proportion: 5 wt.% of Y_2SiO_5). EDS analysis confirm the presence of several crystallised phases after 7 minutes of interaction (Figure 7a): yttrium monosilicate MSY, disilicate DSY, oxide Y_2O_3, and cyclosilicate $Ca_3Y_2(Si_3O_9)_2$. However, the characterization of the initial MSY powder (see paragraph 2.1) has revealed that the powder is not pure, as it also contains significant amounts of DSY and Y_2O_3. As these three phases are present in the initial powder, it is impossible to conclude about their precipitation or dissolution in the CAS melt after 7 minutes of interaction at 1300°C. However, the cyclosilicate phase, which is not present in the initial mix and contains some elements brought by the liquid (Ca Si), precipitates during the first 7 minutes. After 1 hour of interaction, the apatite phase $Ca_2Y_8(SiO_4)_6O_2$ is detected (Figure 7b), and MSY and DSY are no longer observed. After 4 hours of interaction between MSY and CAS (Figure 7c), cyclosilicate and apatite precipitates are still present in the melt. The cyclosilicate surrounds apatite, as observed in the sample where yttrium is initially brought by DSY (Figure 3c) or by Y_2O_3 (Figure 6c). For all durations of the interaction between MSY and CAS, cyclosilicate is the phase in equilibrium with the liquid. Compared to DSY-CAS interaction, fewer aggregates are observed, and as for Y_2O_3-CAS interaction, homogeneous morphology of apatite is observed, with no other phase in the core of the precipitated grains.

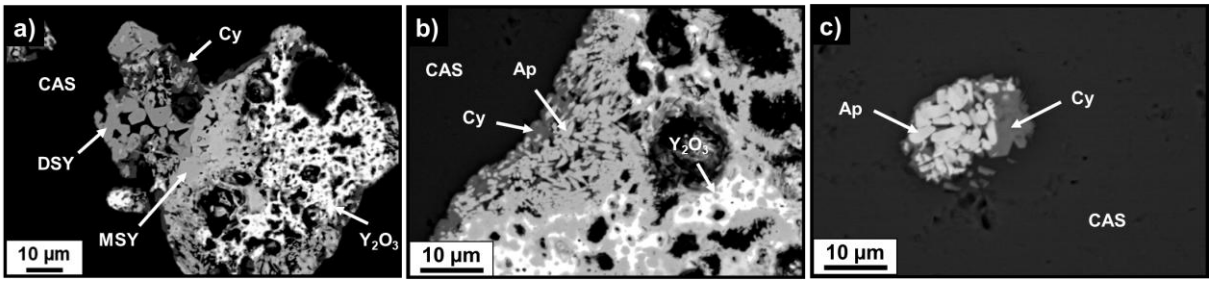

Figure 7. SEM micrographs (Back Scattered Electrons mode) of a CAS samples added with 5 wt.% Y_2SiO_5 (MSY) after 7 min (a), 1 h (b) and 4 h (c) of interaction at 1300°C.

4. Discussion

For all yttrium sources (5 wt.% of monosilicate, disilicate or oxide), the phase at equilibrium with a CAS melt at 1300°C is the cyclosilicate phase. In all cases, after 4 hours of interaction, almost all precipitates are dissolved in the melt. The preferential growth of cyclosilicate over

apatite seems to be observed, the amount of cyclosilicate becoming larger than the amount of apatite with time in all cases.

Figure 2 shows that the nature of rare-earth source has very low influence on the position of the theoretical points of initial mixes: they are all located in the liquid zone which is in equilibrium with the cyclosilicate phase. This explains the local liquid-cyclosilicate equilibria observed for the three types of samples after short term interactions with CAS, and the important amount of dissolved species after 4 hours of interaction.

The main morphologic characteristics of the precipitated apatite and cyclosilicate phases after 4 hours of interaction with CAS at 1300°C are reported in Table 2.

Table 3. Morphology of the precipitated phases after 4 h of interaction at 1300°C with CAS when starting from 5 wt.% of $Y_2Si_2O_7$, Y_2O_3 and Y_2SiO_5 (l = length; Φ = diameter).

	Yttrium source		
	Yttrium disilicate $Y_2Si_2O_7$	Yttrium oxide Y_2O_3	Yttrium monosilicate Y_2SiO_5
Apatite	acicular +++ needles with SiO_2 core 2 µm < l < 20 µm 1 µm < Φ < 5 µm	acicular + dense needles 0.5 µm < l < 3 µm 0,2 µm < Φ < 1.5 µm	acicular ++ dense needles 4 µm < l < 10 µm 1 µm < Φ < 4 µm
Cyclosilicate	coarse precipitates 5 µm < l < 50 µm	coarse precipitates 1 µm < l < 10 µm	coarse precipitates 1 µm < l < 8 µm

It has been shown that the apatite phase formed when starting from yttrium disilicate $Y_2Si_2O_7$ exhibits a specific morphology with a dark contrast in the core of the precipitated needles (Figure 3, Table 3). This is attributed to the presence of SiO_2 (Figure 5, Table 2), which can be explained through the chemical reaction leading to apatite formation when starting from yttrium disilicate. Indeed, Eq. 1 shows that this reaction consumes CaO from the melt and simultaneously releases SiO_2, as already seen in the literature [16,17]. Consequently, some proportion of this silica produced by the reaction can be found trapped in the core of the apatite needles.

$$4\ Y_2Si_2O_7 + 2\ CaO \rightarrow Ca_2Y_8(SiO_4)_6O_2 + 2\ SiO_2 \quad \text{(Eq. 1)}$$

This morphology has previously been encountered in the literature, [15,16,20,21,27]. However, the presence of silica in the core of the precipitates is clearly identified here thanks to STEM analysis, and the precipitation mechanism is determined.

The amorphous phase consisting in yttria-enriched CAS (zone 2, Figure 5, Table 2) exhibits a light enrichment in SiO_2 and a more substantial impoverishment in CaO compared to the initial CAS composition. This can be explained by considering that this melt is in contact with both apatite (formed with CaO consumption and SiO_2 release, see Eq. 1) and cyclosilicate (formed with CaO and SiO_2 consumption from the melt, see Eq. 2).

$$Y_2Si_2O_7 + 3\ CaO + 4\ SiO_2 \rightarrow Ca_3Y_2(Si_3O_9)_2 \quad \text{(Eq. 2)}$$

The STEM study after 1 hour of interaction between yttrium disilicate and CAS evidences a local 3-phases equilibrium between liquid, cyclosilicate and apatite at the center of the precipitated agglomerates. This 3-phases equilibrium is consistent with our previous study

[26], in which similar results are observed when the ternary CaO-SiO_2-$YO_{1.5}$ diagram is modified through addition of more than 9 mol.% of Al_2O_3 to the system. Furthermore, the presence of SiO_2 in the core of the apatite needle illustrate the existence of a 2-phase equilibrium between apatite and SiO_2 as shown in the ternary diagram proposed by Summers et al. [16]. This analysis also shows that cyclosilicate grains surround apatite grains deep in the sample (Figure 4b), and not only in the plan corresponding to the micrograph in Figure 4a.

A different apatite morphology is observed when starting from yttrium monosilicate MSY or yttrium oxide Y_2O_3, as the composition is homogeneous (no chemical contrast in the core of the apatite needles, as seen on Figures 6 and 7). Furthermore, as shown in Table 3, the precipitated apatites has lower acicularity in both cases, since the length of the needles is much shorter. An explanation might be found when considering the reaction leading to the precipitation of apatite when starting from Y_2O_3 (Eq. 3) and from Y_2SiO_5 (Eq. 4).

$$4\ Y_2O_3 + 2\ CaO + 6\ SiO_2 \rightarrow Ca_2Y_8(SiO_4)_6O_2 \qquad \text{(Eq. 3)}$$

$$4\ Y_2SiO_5 + 2\ CaO + 2\ SiO_2 \rightarrow Ca_2Y_8(SiO_4)_6O_2 \qquad \text{(Eq. 4)}$$

In the same way, the cyclosilicate precipitates are significantly less coarse (10 µm maximum vs. 50 µm when starting from $Y_2Si_2O_7$), the reactions leading to cyclosilicate precipitation being reported in Eq. 5 (when starting ggrom Y_2O_3) and Eq. 6 (when starting from Y_2SiO_5).

$$Y_2O_3 + 3\ CaO + 6\ SiO_2 \rightarrow Ca_3Y_2(Si_3O_9)_2 \qquad \text{(Eq. 5)}$$

$$Y_2SiO_5 + 3\ CaO + 5\ SiO_2 \rightarrow Ca_3Y_2(Si_3O_9)_2 \qquad \text{(Eq. 6)}$$

By comparing Eq. 3 and Eq. 4 (starting from yttrium oxide and yttrium monosilicate respectively) to Eq 1 (starting from yttrium disilicate), it can be seen that for the formation of 1 mole of apatite, the same amounts of CaO are required in all cases (2 moles), but no silica is required when starting from disilicate. This might explain the higher reactivity in the case of disilicate. Considering the apatite growth thanks to the favored ionic conduction in 2a sites [29] the higher acicularity of precipitated apatite can be linked to its faster growth. The same reasoning can be made for the precipitation of cyclosilicate by comparing Eq. 5 and Eq. 6 (starting from starting from yttrium oxide and yttrium monosilicate respectively) to Eq. 2 (starting from yttrium disilicate). The only difference between the three cases is that yttrium disilicate consumes less reagents from the melt (same amount of CaO but less SiO_2) than yttrium oxide and yttrium monosilicate to form the cyclosilicate phase, thus leading to a favored growth and significantly coarser grains.

Furthermore, the equations of apatite formation when starting from Y_2O_3 and Y_2SiO_5 (Eq. 3 and Eq. 4) show that silica is never released in both cases. The literature also shows precipitation of homogeneous apatite when starting from yttrium monosilicate [2,30,31]. These reactions emphasize that the mechanisms involved in the formation of rare-earth rich phases depend on the source providing the rare-earth element, since the proportion of consumed or released CaO and SiO_2 are not the same, thus influencing the evolution of the melt composition. These mechanisms have been previously observed by comparing different rare-earth sources [17,19,21,22], and melts with different compositions (i.e. various abilities to provide calcium) [16,17,21].

EPMA measurements were performed in the melt close to the precipitates and are reported in Figure 8.

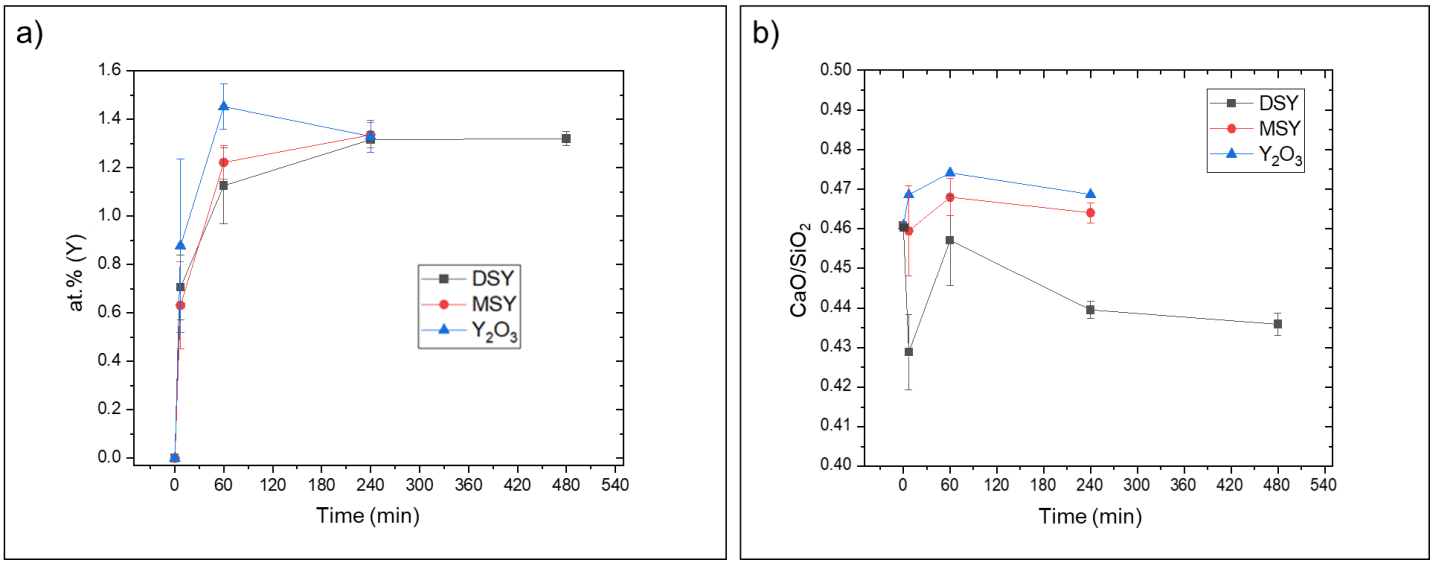

Figure 8. Evolution with time of the yttrium solubility (a) and of the CaO/SiO_2 ratio (b) at 1300°C in CAS added with DSY(5 wt.%), MSY (5 wt.%) and Y_2O_3 (5 wt.%).

Figure 8(a) compares the evolution with time of yttrium content in the melt for the three types of yttrium sources (oxide, monosilicate and disilicate). In all cases, the yttrium content increases very fast. Standard deviations tend to decrease with time, proving that all systems tend to get close to a local thermodynamic equilibrium [32]. Starting from 4 hours of interaction, all solubilities tend to the same value of around 1.3 at.%(Y). It has been shown that in the three cases, the melt is in equilibrium with the same cyclosilicate phase (which is consistent with the phase diagram in Figure 2), thus leading to the same solubility value for yttrium.

Figure 8(b) describes the evolution of the CaO/SiO_2 ratio in the melt for the three types of yttrium source, close to the precipitated phases. Different trends are observed, showing different evolutions of liquid composition due to the dissolution/precipitation mechanisms. The starting point is at $CaO/SiO_2 = 0.46$ (Table 1). When starting with DSY, the decrease at 7 minutes is due to its dissolution which releases SiO_2 thus involving an increase of its content in the melt. The higher long term values of the CaO/SiO_2 ratio is measured when starting from Y_2O_3, and the lowest when starting from yttrium disilicate DSY. This can be explained by the amount of silica brought by the yttrium source, which is higher in the case of disilicate DSY compared to monosilicate MSY. Indeed, a higher amount of silica dissolved in the melt induces a decrease of the CaO/SiO_2 ratio. Furthermore, the reactions leading to the formation of rare-earth rich phases are also different. Similar trends are observed with different CaO/SiO_2 ratios values. Indeed, precipitation of apatite and cyclosilicate consume and release different amounts of CaO and SiO_2, which depend on the source of yttrium and the nature of the precipitated phases.

5. Conclusions

The interactions between a simplified ternary silicate melt CaO-Al_2O_3-SiO_2 and three rare-earth sources (Y_2O_3, Y_2SiO_5 and $Y_2Si_2O_7$) have been investigated at 1300°C with a 5wt.% load. These conditions allow the observation of the local interactions between the phases and the melt. In all cases, fast precipitation of apatite $Ca_2Y_8(SiO_4)_6O_2$ has been observed, with long term formation of cyclosilicate $Ca_3Y_2(Si_3O_9)_2$ to the detriment of apatite. The melt is always in equilibrium with cyclosilicate, consistently with the phase diagram proposed in our previous work [26]. This consistency is of great interest as it allows to have similar approaches when considering rare-earth elements other than yttrium, or more complex melts closer to real CMAS compositions.

Precipitation of apatite always occurs with an acicular shape. However, a specific case is encountered when yttrium is brought by disilicate, as the core of the apatite needles exhibits a different chemical composition with the presence of silica. This has been discussed regarding the chemical mechanisms leading to apatite precipitation, and their influence on the melt composition. Since yttrium disilicate is the silica-rich rare-earth source here, it is the only case where apatite formation and growth lead to the release of silica. The higher reactivity of yttrium disilicate has also been emphasized due to its lower consumption of elements brought by the melt. Evaluation of the melt composition close to the precipitates shows evolutions of the Ca/Si ratio were consistent with the proposed reaction mechanisms and phases at equilibrium: as expected, they are not the same for the different yttrium sources used here. It is thus shown that the same equilibrium state (nature of the phases at equilibrium) can exhibit different morphologies due to the involved chemical reactions.

Acknowledgements

The authors gratefully acknowledge the Microscopies, Microprobes and Metallography Competence Center of the IJL for performing EPMA measurements and STEM observations.

References

[1] L. Guo, W. He, W. Chen, Z. Xue, J. He, Y. Guo, Y. Wu, L. Gao, D. Li, Z. Zhang, L. Wei, Y. Gao, T. Zhang, J. Qiao, Q. Li, H. Guo, Progress on high temperature protective coatings for aero-engines, Surf. Sci. Technol. 2023 1-6, https://doi.org/10.1007/s44251-023-00005-6

[2] K.M. Grant, S. Krämer, G.G.E. Seward, C.G. Levi, Calcium–Magnesium Alumino-Silicate Interaction with Yttrium Monosilicate Environmental Barrier Coatings, J. Am. Ceram. Soc. 93 (2010) 3504–3511, https://doi.org/10.1111/j.1551-2916.2010.03916.x

[3] S. Krämer, J. Yang, C.G. Levi, Infiltration-inhibiting reaction of gadolinium zirconate Thermal Barrier Coatings with CMAS melts, J. Am. Ceram. Soc. 91 (2008) 576–583, https://doi.org/10.1111/j.1551-2916.2007.02175.x

[4] L. Guo, H. Xin, Y. Li, Y. Yu, Z. Yan, C. Hu, F Ye, Self-crystallization characteristics of calcium-magnesium-alumina- silicate (CMAS) glass under simulated conditions for thermal barrier coating applications, , J. Eur. Ceram. Soc. 40 (2020) 5683–5691, https://doi.org/10.1016/j.jeurceramsoc.2020.07.025

[5] J. Liu, L. Zhang, Q. Liu, L. Cheng, Y. Wang, Calcium–magnesium–aluminosilicate corrosion behaviors of rare-earth disilicates at 1400°C, J. Eur. Ceram. Soc. 33 (2013) 3419–3428, http://dx.doi.org/10.1016/j.jeurceramsoc.2013.05.030

[6] D.L. Poerschke, T.L. Barth, C.G. Levi, Equilibrium relationship between thermal barrier oxides and silicate melts, Acta Mater. 120 (2016) 302-314, http://dx.doi.org/10.1016/j.actamat.2016.08.077

[7] L. Guo, Y. Li, K. Yan, Corrosion behavior of $Gd_2Zr_2O_7$ thermal barrier coatings under Fe-containing environmental sediment attack, J. Adv. Ceram. 13 (2024) 447-462, https://doi.org/10.26599/JAC.2024.9220867

[8] Y. Dong, K. Ren, Q. Wang, G. Shao, Y. Wang, Interaction of multicomponent disilicate $(Yb_{0.2}Y_{0.2}Lu_{0.2}Sc_{0.2}Gd_{0.2})_2Si_2O_7$ with molten calcia-magnesia-aluminosilicate, J. Adv. Ceram. 11 (2022) 66-74, https://doi.org/10.1007/s40145-021-0517-7.

[9] V.L. Wiesner, B.J. Harder, A. Garg, N.P. Bansal, Molten calcium–magnesium–aluminosilicate interactions with ytterbium disilicate environmental barrier coating, J. Mater. Res. 35 (2020) 2346-2357, https://doi.org/10.1557/jmr.2020.211.

[10] F. Perrudin, C. Rio, M.H. Vidal-Setif, C. Petitjean, P.J. Panteix, M. Vilasi, Gadolinium oxide solubility in molten silicate: dissolution mechanism and stability of $Ca_2Gd_8(SiO_4)_6O_2$ and $Ca_3Gd_2(Si_3O_9)_2$ silicate phases, J. Eur. Ceram. Soc. 37 (2017) 2657-2664, http://dx.doi.org/10.1016/j.jeurceramsoc.2017.02.022

[11] F. Perrudin, M.H. Vidal-Setif, C. Rio, C. Petitjean, P.J. Panteix, M. Vilasi, Influence of rare earth oxides on kinetics and reaction mechanisms in CMAS silicate melts, J. Eur. Ceram. Soc 39 (2019) 4223-4232, https://doi.org/10.1016/j.jeurceramsoc.2019.06.036

[12] L. Guo, B. Zhang, Y. Gao, K. Yan, Interaction laws of RE_2O_3 and CMAS and rare earth selection criterions for RE-containing thermal barrier coatings against CMAS corrosion, Corros. Sci. 226 (2024) 111689, https://doi.org/10.1016/j.corsci.2023.111689

[13] J.C. Elliott, Structure and Chemistry of the Apatites and Other Calcium Orthophosphates, Elsevier (1994).

[14] D.L. Poerschke, T.L. Barth, O. Fabrichnaya, C.G. Levi, Phase equilibria and crystal chemistry in the calcia–silica–yttria system, J. Eur. Ceram. Soc. 36 (2016) 1743–1754, https://doi.org/10.1016/j.jeurceramsoc.2016.01.046

[15] V.L. Wiesner, B.J Harder, N.P. Bansal, High-temperature interactions of desert sand CMAS glass with yttrium disilicate environmental barrier coating materials, Ceram. Int. 44 (2018) 22738-22743, https://doi.org/10.1016/j.ceramint.2018.09.058

[16] W.D. Summers, D.L. Poerschke, D. Park, J.H. Shaw, F.W. Zok, C.G. Levi, Roles of composition and temperature in silicate deposit-induced recession yttrium disilicate, Acta Mater. 160 (2018) 34-46, https://doi.org/10.1016/j.actamat.2018.08.043

[17] H. Zhao, B.T. Richards, C.G. Levi, H.N.G. Wadley, Molten silicate reactions with plasma sprayed ytterbium silicate coatings, Surf. Coat. Tech. 288 (2016) 151-162, http://dx.doi.org/10.1016/j.surfcoat.2015.12.053

[18] L.R. Turcer, A.R. Krause, H.F. Garces, L.Zhang, N.P. Padture, Environmental-barrier coating ceramics for resistance against attack by molten calcia-magnesia-aluminosilicate (CMAS) glass: Part II, β-$Yb_2Si_2O_7$ and β-$Sc_2Si_2O_7$, J. Eur. Ceram. Soci. 38 (2018) 3914-3924, https://doi.org/10.1016/j.jeurceramsoc.2018.03.010

[19] F. Stolzenburg, M.T. Johnson, K.N. Lee, N.S. Jacobson, K.T. Faber, The interaction of calcium-magnesium-aluminosilicate with ytterbium silicate environmental barrier materials, Surf. Coat. Tech. 284 (2015) 44-50, http://dx.doi.org/10.1016/j.surfcoat.2015.08.069

[20] J.L. Stokes, B.J. Harder, V.L. Wiesner, D.E. Wolfe, High-temperature thermochemical interactions of molten silicates with $Yb_2Si_2O_7$ and $Y_2Si_2O_7$ environmental barrier coating materials, J. Eur. Ceram. Soc. 39 (2019) 5059-5067, https://doi.org/10.1016/j.jeurceramsoc.2019.06.051

[21] J.L. Stokes, B.J. Harder, V.L. Wiesner, D.E. Wolfe, Effect of crystal structure and cation size on molten silicate reactivity with environmental barrier coating materials, J. Am. Ceram. Soc. 103 (2020) 622-634, https://doi.org/10.1111/jace.16694

[22] N.L. Ahlbord, D. Zu, Calcium-magnesium aluminosilicate (CMAS) reactions and degradation mechanisms of advanced environmental barrier coatings, Surf. Coat. Tech. 237 (2013) 79-87, http://dx.doi.org/10.1016/j.surfcoat.2013.08.036

[23] B. Zhou, Y. Wu, X. Ke, Q. Zhou, Y. Cui, C. Wang, M. Guo, J. Jiao, Resistance of ytterbium silicate environmental barrier coatings against molten calcium-magnesium-aluminosilicate (CMAS): a comprehensive study, Surf. Coat. Tech. 479 (2024) 130540, https://doi.org/10.1016/j.surfcoat.2024.130540

[24] L.R. Turcer, A.R. Krause, H.F. Garces, L.Zhang, N.P. Padture, Environmental-barrier coating ceramics for resistance against attack by molten calcia-magnesia-aluminosilicate (CMAS) glass: part I, $YAlO_3$ and γ-$Y_2Si_2O_7$, J. Eur. Ceram. Soc. 38 (2018) 3905-3913, https://doi.org/10.1016/j.jeurceramsoc.2018.03.021

[25] C.G. Levi, J.W. Hutchinson, M.H. Vidal-Setif, C.A. Johnson, Envrionmental degradation of thermal-barrier coatings by molten deposits, MRS Bull. 37 (2012) 932-941, https://doi.org/10.1557/mrs.2012.230

[26] J. Bonnal, S. Mermoul, C. Petitjean, P.J. Panteix, D. Bonina, C. Gendarme, S. Arnal, M. Vilasi, A thermodynamic study of the influence of the Al_2O_3 content on the CaO-SiO_2-$YO_{1.5}$ system, J. Eur. Ceram. Soc. 44 (2024) 4160-4169, https://doi.org/10.1016/j.jeurceramsoc.2024.01.072

[27] D.L. Poerschke, J.H. Shaw, N. Verma, F.W. Zok, C.G. Levi, C.G., Interaction of yttrium disilicate environmental barrier coatings with calcium-magnesium-iron alumino-silicate melts, Acta Mater. 145 (2018) 451–461, https://doi.org/10.1016/j.actamat.2017.12.004

[28] V.L. Wiesner, D. Scales, N.S. Johnson, B.J. Harder, A. Garg, N.P. Bansal, Calcium–magnesium aluminosilicate (CMAS) interactions with ytterbium silicate environmental barrier coating material at elevated temperatures, Ceram. Int. 46 (2020) 16733–16742, https://doi.org/10.1016/j.ceramint.2020.03.249

[29] P.J Panteix, E. Béchade, I. Julien, P. Abélard, D. Bernache-Assollant, Influence of anionic vacancies on the ionic conductivity of silicated rare earth oxyapatites, Mater. Res. Bull. 43 (2008) 1223-1231, https://doi.org/10.1016/j.materresbull.2007.05.030

[30] A. Rose, J.J. Gomez Chavez, P. Mechnich, K. Kelm, U. Schulz, R. Naraparaju, Novel magnetron sputtered yttrium-silicon-iron oxide as CMAS resistant top coat material for environmental barrier coatings, Corros. Sci. 215 (2023) 111053, https://doi.org/10.1016/j.corsci.2023.111053

[31] W.D. Summers, D.L. Poerschke, A.A. Taylor, A.R. Ericks, C.G. Levi, F.W. Zok, Reactions of molten silicate deposits with yttrium monosilicate, J. Am. Ceram. Soc. 103 (2023) 2919–2932, https://doi.org/10.1111/jace.16972

[32] T.K. Abdullah, C. Petitjean, P.J. Panteix, C. Rapin, M. Vilasi, Z. Hussain, A. Abdul Rahim, Dissolution equilibrium of chromium oxide in a soda lime silicate melt exposed to oxidizing and reducing atmospheres, Mater. Chem. Phys. 142 (2013) 572–579, http://dx.doi.org/10.1016/j.matchemphys.2013.07.055

Figure captions

Figure 1. X-ray diffraction patterns of reagents powders of yttrium oxide Y_2O_3 (a), yttrium disilicate $Y_2Si_2O_7$ (b), and yttrium monosilicate Y_2SiO_5 (c).

Figure 2. Theoretical compositions of the CAS samples added with 5 wt.% of DSY, MSY and Y_2O_3 reported in the modified ternary phase diagram $CaO\text{-}SiO_2\text{-}YO_{1.5}$ added with 9 mol.% Al_2O_3 at 1300°C [26].

Figure 3. SEM micrographs (Back Scattered Electrons mode) of a CAS samples added with 5 wt.% $Y_2Si_2O_7$ (DSY) after 7 min (a), 1 h (b) and 4 h (c) of interaction at 1300°C.

Figure 4. SEM micrographs (Secondary Electrons mode) of a CAS sample added with 5 wt.% (DSY) after 1 h of interaction at 1300°C (a) and of the FIB sample extracted from the hatched area (b)

Figure 5. STEM-BF micrograph of the center of an agglomerate of a CAS sample added with 5 wt.% (DSY) after 1 h of interaction at 1300°C (a), and diffraction patterns of zone 1 (b), zone 2 (c), and of apatite (d) and cyclosilicate (e) phases.

Figure 6. SEM micrographs (Back Scattered Electrons mode) of CAS samples added with 5 wt.% Y_2O_3 after 7 min (a), 1 h (b) and 4 h (c) of interaction at 1300°C.

Figure 7. SEM micrographs (Back Scattered Electrons mode) of CAS samples added with 5 wt.% Y_2SiO_5 (MSY) after 7 min (a), 1 h (b) and 4 h (c) of interaction at 1300°C.

Figure 8. Evolution with time of the yttrium solubility (a) and of the CaO/SiO_2 ratio (b) at 1300°C in CAS added with DSY(5 wt.%), MSY (5 wt.%) and Y_2O_3 (5 wt.%).